Rend. Lincei Mat. Appl. (Online first)
DOI 10.4171/RLM/1003

Published by EMS Press

Mathematical Biology. – *Traveling waves and free boundaries arising in tumor angiogenesis*, by Antonio Fasano and Carmela Sinisgalli, communicated on 10 November 2022.

Abstract. – In a paper appeared in 2021, a mathematical model was developed for tumor invasion with vessel cooption, including a fine analysis of angiogenesis driven by chemotaxis. Numerical solutions in spherical symmetry revealed that a traveling wave sets in. Results were in agreement with experimental data. In the present paper, we introduce some nontrivial changes in the model and we further analyze the structure of the solutions as well as their dependence on some critical biological parameters, emphasizing for instance which are the most active zones where angiogenesis takes place. Moreover, we propose an alternative model characterized by the presence of a free boundary (playing the role of the invasion front), showing that the new formulation (which is advantageous from the computational point of view) matches the results of the previous model for some biologically significant range of the parameters.

Keywords. – Modeling vascularized tumor growth, angiogenesis, chemotaxis, tumor invasion, traveling waves, Fickian diffusion.

2020 Mathematics Subject Classification. – Primary 35K57; Secondary 35C07, 35R35, 35Q92, 92C17.

1. Introduction

At its initial stage, a tumor is small enough to be fed by nearby blood vessels via the efficient mechanism of diffusion. Capillaries may provide oxygen and nutrients to surrounding cells up to a distance of about 100–200 μm (this explains why billions of them are needed in the human body). A tumor that has grown to a size of, say, 1 mm diameter finds itself in critical conditions, since cells in its innermost core become hypoxic. Hypoxic cells react emitting molecules (tumor angiogenesis factors (TAFs)) which diffuse to the blood vessels next to the tumor, stimulating the branching of new vessels. The new vessels eventually reach the tumor creating a network providing all the tumor needs for further growth. Such a phenomenon is called angiogenesis [1]. Since the discovery of angiogenesis, an extensive literature has been produced, also in the field of mathematical modeling of tumor-induced angiogenesis (e.g. [4, 5, 11]). Here we confine to mentioning a few examples in different classes of models:

(i) continuous models [3, 12, 19, 20];

(ii) discrete deterministic models [2, 18];

(iii) discrete stochastic models [2, 16, 19, 21].

The mechanism that drives the forming vessels towards the tumor is chemotaxis, since the epithelial cells forming the new vessels follow the trail set by TAF, approaching the zone of its maximal concentration, i.e., the tumor. The standard model for chemotaxis, as laid in the seminal papers [14, 17], attributes to cells a velocity proportional to the gradient of the chemotactic agent concentration. However, such an approach is not suitable when dealing with angiogenesis because of various reasons. First of all, in such a simple setting the corresponding chemotactic velocity can reach arbitrarily large values, which is not our case since the new vessels progress thanks to cells which proliferate but are not free to move around, being adherent to the new growing structure. Moreover, it is not true that cells orienting themselves in the field of the TAF concentration align exactly along the gradient direction, because, on the contrary, they tend to change their orientation according to a stochastic mechanism. Thus, besides the various phenomena concurring in the angiogenesis process, the chemotactic aspect needs particular attention. The extensive study recently performed in [9] was based on a fine analysis of chemotaxis accounting both for the existence of an intrinsic physiological bound to cells velocity, and for the disturbance created by the spontaneous random change of direction exhibited by migrating cells. The model in [9] will be referred to as G-2021.

Numerical simulations performed in spherical symmetry provided results that match reasonably well available experimental data of microvasculature density. Moreover, they strongly suggest that the tumor invades the host tissue proceeding as a traveling wave (TW).

The first tumor growth model yielding a TW solution (in plane symmetry) was the one by Gatenby and Gawlinski [10], further analyzed from the mathematical point of view in [6], and very recently considered in a reduced form to prove existence and non-existence of invasive fronts [8]. The model in [10] (in the sequel referred to as the GG model) was not concerned with angiogenesis, but included the tumor aggression to the host tissue through the acidic environment created by the tumor cell metabolism. In the following, we will emphasize similarities and differences between the GG model and the G-2021 model.

We start by summarizing the G-2021 model, at the same time introducing some changes to make it closer to reality. While in the original G-2021 model only tumor cells were allowed to diffuse, now we assume that, after tumor aggression, healthy cells too start diffusing in the advancing front region and that dead cells are also subject to diffusion. The consequence is a non-negligible acceleration of the tumor invasion. Such an updated model will be referred to as G-2022 model.

Two main goals will be pursued in this paper.

(1) Investigating the TW structure of the solutions to G-2022 and their dependence on some critical parameters. It will be seen that in the limit case of fast decay of dead cells, such TWs are characterized by a rather sharp propagating front and some of their properties can be predicted analytically and tested numerically. The TW propagation velocity will be shown to increase if the tumor is supposed to be more aggressive to the host tissue.

(2) The study of the TW behavior of the solutions suggests that the limit case of the G-2022 model is actually a free boundary (FB) model, which will be formulated and numerically investigated. In this FB model, the healthy cells die instantly when reached by tumor cells, so that the tumor and the healthy tissues are neatly separated by the tumor propagation front (the FB). This is of course an extrapolation but does have a physical meaning if we consider that "instantly" actually means "in a time which is very short compared to the natural timescale of the tumor progression". It will turn out that the FB formulation has some advantage from the computational point of view.

2. Summary of the model

We report the model equations directly in the spherical symmetry. The tumor expands from an initially avascular sphere (radius 0.02–0.03 cm), hosted by a healthy tissue. The domain considered is a sphere of radius $R \geq 1$ cm that in any case we suppose sufficiently larger than the tumor outer boundary. The model includes many quantities, grouped as follows:

(I) cell densities of the main populations: n (tumor), h (host), m (dead cells);

(II) cell densities of the vascular system: v_h, v_a (host tissue vasculature); v, w, z (tumor vasculature);

(III) chemical concentrations: σ (oxygen), P (TAF *interstitial* concentration).

We add some clarification. To each cell density (cells number p.u. volume) we may associate a corresponding volume fraction multiplying it by the cell volume V_c. For simplicity, all cells are assumed to have the same volume. Volume fractions will be denoted by the symbols ϕ_i and the total cells volume fraction ϕ is not allowed to exceed a value $\phi^\star < 1$ (taking into account the space occupied by the extracellular matrix). All terms expressing cells mobility and proliferation will contain the limiting factor

$$B(\phi) = \left(1 - \frac{\phi}{\phi^*}\right)^p, \quad p \geq 1,$$

expressing a crowding effect.

The host tissue microvasculature includes two variable components: capillaries and venules (total density v_h). The arteriolar component v_a is taken constant in the present model in view of its negligible dynamics [15]. Healthy cells, including the ones of the venous vasculature, are attacked by the tumor. The tumor vasculature is made by three types of cells: the ones forming mature vessels (v), the final stage of two temporary populations consisting of the sprout stalk (z) and the sprout tip (w) cells. The interplay between these classes is not simple and in the model under consideration it was assumed for simplicity that tip cells are generated as the result of the TAF stimulus on the existing vasculature and that in turn they generate one tip and one stalk cells. Tip cells are the ones sensing TAF and selecting the growth direction of the forming vessel.

It must also be stressed that there are several different kinds of TAFs (a fact clearly complicating anti-angiogenic therapies). The model includes just one as a representative of the whole class. The TAF action enters the model through the fraction ψ of TAF engaged endothelial cell receptors, which is related to P by the formula

$$\psi = \frac{P}{K_d + P}.$$

Indexed symbols like K_i (and similarly $A_i, \mu_i, \delta_i, \lambda_i$) will denote positive experimental constants. Note that $\nabla\psi$ is parallel to ∇P.

That said, let us review and comment on the model differential system.

Tumor cell balance

$$\frac{\partial n}{\partial t} = \frac{1}{r^2}\frac{\partial}{\partial r}\Big(r^2 D_n B(\phi)\frac{\partial n}{\partial r}\Big) + B(\phi)\chi(\sigma)n - \mu_n(\sigma)n, \tag{2.1}$$

where diffusivity D_n and proliferation rate χ are limited by the crowding factor B. In addition, both proliferation χ and death rate μ_n are dependent on the oxygen concentration:

$$\chi(\sigma) = A_\chi \frac{\sigma}{K_\chi + \sigma},$$

$$\mu_n(\sigma) = \begin{cases} \bar{\mu}_n cos^2\big(\frac{\pi}{2}\frac{\sigma}{\bar{\sigma}_n}\big) + \mu_0, & \sigma \in [0, \bar{\sigma}_n], \\ \mu_0, & \sigma \in (\bar{\sigma}_n, +\infty), \end{cases}$$

where $\bar{\sigma}_n$ is a critical oxygen concentration below which death rate is larger.

Healthy cells balance

$$\frac{\partial h}{\partial t} = \frac{1}{r^2}\frac{\partial}{\partial r}\left(r^2 D_h B(\phi)\frac{\partial h}{\partial r}\right) - \delta_h n\, h - \mu_h(\sigma)h, \tag{2.2}$$

where the diffusive term (absent in model G2021) accounts for cell mobility; moreover, healthy cells die as a consequence of tumor aggression, whose intensity is specified by the coefficient δ_n, or by hypoxia, according to the following death rate:

$$\mu_h(\sigma) = \begin{cases} \overline{\mu}_h cos^2\left(\frac{\pi}{2}\frac{\sigma}{\overline{\sigma}_h}\right), & \sigma \in [0, \overline{\sigma}_h], \\ 0, & \sigma \in (\overline{\sigma}_h, +\infty), \end{cases}$$

with $\overline{\sigma}_h > \overline{\sigma}_n$ because tumor cells can switch to anaerobic metabolism (of which lactic acid is a byproduct, lowering the local pH).

Dead cells balance

$$\frac{\partial m}{\partial t} = \frac{1}{r^2}\frac{\partial}{\partial r}\left(r^2 D_m B(\phi)\frac{\partial m}{\partial r}\right) + \mu_n(\sigma)n + \mu_h(\sigma)h + \mu_w w + \mu_z z + \mu_v v + \delta_h n h + \delta_{v_h} n v_h - \lambda_m m, \tag{2.3}$$

This class collects all cells that die for various reasons. The first term again accounts for diffusive mobility (absent in model G2021), whereas the last term expresses degradation.

Tumor attack to healthy vasculature

$$\frac{\partial v_h}{\partial t} = -\delta_{v_h} n\, v_h. \tag{2.4}$$

Oxygen diffusion-consumption

$$0 = D_\sigma \frac{1}{r^2}\frac{\partial}{\partial r}\left(r^2\frac{\partial \sigma}{\partial r}\right) + \gamma_h v_h(\sigma_h^* - \sigma) + \gamma_v v(\sigma_v^* - \sigma) - H_n(\sigma)n - H_h(\sigma)h. \tag{2.5}$$

Equation (2.5) is in the quasi-steady form because the oxygen diffusivity D_σ is so large that the time scale of this phenomenon is much shorter than the typical time scale of all other processes involved. Moreover, oxygen diffuses throughout the medium and this explains the absence of the limiting factor B in the first term. The source terms represent oxygen supply by the vasculature and the consumption rates by tumor and healthy cells are as follows:

$$H_i(\sigma) = A_{Hi}\frac{\sigma}{K_{Hi} + \sigma}, \quad i = n, h.$$

TAF diffusion

$$\frac{\partial}{\partial t}\left((\phi_P^* - \phi)P\right) = \frac{1}{r^2}\frac{\partial}{\partial r}\left(D_P(\phi_P^* - \phi)\frac{\partial P}{\partial r}\right) + \pi_P(\sigma)n - C_P(P)(v_h + v + z + w) - \lambda_P P(\phi_P^* - \phi). \tag{2.6}$$

We recall that P denotes the interstitial concentration, so $P(\phi_P^* - \phi)$ is instead the bulk TAF concentration, where $(\phi_P^* - \phi)$ is the volume fraction available to TAF (clearly larger than the one available to cells). Note that the diffusion term has the form typical of diffusion through porous media, since only ∇P is responsible for TAF diffusion through interstices, while $\nabla\phi$ has no influence on it. The last term expresses natural decay; the production term has the coefficient $\pi_P(\sigma)n$, where

$$\pi_P(\sigma) = A_\pi \frac{K_\pi - \sigma}{K_\pi + \sigma},$$

and consumption by cells sensors is regulated by the coefficient

$$C_P(P) = A_C \frac{P}{K_d + P}.$$

Evolution of tumor vasculature

(a) Tip sprout cells.

$$\begin{aligned}\frac{\partial w}{\partial t} = {} & \frac{1}{r^2}\frac{\partial}{\partial r}\left(r^2 D_w(\psi,\phi)\nabla w\right) \\ & - \frac{1}{r^2}\frac{\partial}{\partial r}\left(r^2 u_{tip}(\psi,\phi) q\left(\left|\frac{\partial \psi}{\partial r}\right|\right) \operatorname{sign}\left(\frac{\partial \psi}{\partial r}\right) w\right) \\ & + \alpha(\psi,\phi)(v_h + v) - \kappa_{an}(v_a + v_h + v)w - \mu_w w.\end{aligned} \tag{2.7}$$

(b) Stalk sprout cells.

$$\frac{\partial z}{\partial t} = \beta(\psi,\phi)w - \kappa_{an}(v_a + v_h + v)z - \mu_z z. \tag{2.8}$$

(c) Mature vessels cells.

$$\frac{\partial v}{\partial t} = \kappa_{an}(v_a + v_h + v)(z + w) - \mu_v v. \tag{2.9}$$

Clearly, the system (2.7)–(2.9) is the core of the angiogenesis model and we are going to summarize its main features, going backwards. Equation (2.9) describes how new mature tumor vessels are created as an interaction between tip + stalk cells $(z + w)$ with all mature vasculature structures present at the same location. The last term is natural death. Equation (2.8) shows that stalk cells are generated by tip cells at a rate

$$\beta(\psi,\phi) = A_\beta \psi(1 - \psi)^\nu B(\phi),$$

with $\nu \geq 0$. Actually tip cells are generated and pushed forward by proliferation of adjacent stalk cells, but the present way of writing the equation offers some simplicity

advantage (e.g. modeling haptotaxis is avoided) and has no impact on the final outcome. Taking $\nu > 0$ introduces a limiting effect when many of the receptors are occupied. In equation (2.7) the production term is characterized by the coefficient

$$\alpha(\psi, \phi) = A_\alpha \psi (1 - \psi)^\nu B(\phi),$$

while the first two terms on the right-hand side model chemotaxis. They have a different origin. The term including $\nabla\psi$ resembles the classical convective chemotaxis transport with two basic differences. The first is that, though $\nabla\psi$ selects the direction of velocity, the latter has an intrinsic physiological bound, since cells stick to the forming vessel, so that their velocity cannot exceed

$$u_{tip}(\psi, \phi) = \Lambda\beta(\psi, \phi),$$

where Λ is the average displacement of a tip cell at each cell duplication. Such a feature is guaranteed by the presence of the factor

$$q(|\nabla\psi|) = \frac{|\nabla\psi|}{K_q + |\nabla\psi|}.$$

The diffusion term in (2.7) represents the contribution of the random change of velocity direction. Its derivation is long, complicated and requires several (reasonable) approximations. It is based on typical statistical mechanics arguments. The reader is referred to [9]. The diffusivity D_w turns out to be

$$D_w(\psi, \phi) = \frac{u_{tip}^2(\psi, \phi)}{3\gamma}, \tag{2.10}$$

where γ is the average frequency at which tip cells change their velocity direction. The time $1/\gamma$ is the *persistence time* and a requirement of the model is that it is considerably shorter than the *observation time*, i.e., the time needed to observe some structural change in the tumor. The latter time is of the order of one month (720 h) and we may assume that the permanence time is 10 h ($\gamma = 0.1\,\mathrm{h}^{-1}$). If the permanence time is too small (γ large), the changes are so frequent that they have no effect (D_w tends to zero). If the persistence time is too large, then changes become unobservable and the corresponding term must be dropped (the arguments leading to (2.10) do not apply anymore).

The model is completed by the boundary and the initial conditions as follows. The domain in which the above system has to be solved is a sphere whose radius is much larger than the initial tumor radius. The boundary conditions are $n = w = P = 0$ and $\sigma = \sigma_{\mathrm{ff}}$ (ff = far field), the stationary oxygen concentration in a healthy tissue. Note that only the diffusing quantities need such conditions. For the same species, the symmetry

condition (null derivative with respect to radial coordinate) must be imposed for $r = 0$. The initial conditions, which have to be consistent with the boundary conditions and with the inequality $\phi < \phi^*$, are as follows:

– $m = w = z = v = 0$ (i.e., the tumor is initially avascular),

– at time $t = 0$, n is a positive constant in a small core and rapidly decreases to zero out of it, while h, v_h have the complementary behavior, being zero in the small core and rapidly increasing to the physiological values in the rest of the sphere.

Several a-priori results were obtained in [9], including the study of asymptotic solutions. The said analysis is not influenced by the changes introduced in the G-2022 model.

3. Numerical results

Numerical simulations of the system of equations (2.1), (2.2), (2.3), (2.4), (2.5), (2.6), and (2.7)–(2.9) were performed using the parameters reported in Table 1 and implementing a finite difference method (which is explicit, forward in time, and centered in space) similar to the one of the paper [9].

The typical simulation outcome is summarized in Figures 1 and 2. The evolutions of all local volume fractions are very similar to those presented in [9], with the only visible difference in the (more rounded) spatial profiles of the cell volume fractions ϕ_n, ϕ_h, and ϕ_m, owing to the newly introduced diffusive terms. For completeness, we report the numerical values attained by the model quantities at the final time of the G-2022 model simulation, i.e., at $T = 360$ days: $\sigma = 21.1$ mmHg, $P = 0.27$ nM, $\psi = 0.32$, $\phi_n = 0.64$, $K\phi_v = 1.9 \cdot 10^{-2}$, $K\phi_w = 9.1 \cdot 10^{-4}$, $K\phi_z = 3.6 \cdot 10^{-4}$, $\phi_m = 8.8 \cdot 10^{-2}$, $\phi = 0.75$.

Such results turn out to agree with experimental data of tumor microvasculature density (MVD) in a quite satisfactory way, as in [9]. Defining the tumor MVD as the number of vessels in a 1 mm^2 section of tissue, we can write $\text{MVD} = K\phi_{\text{vasc}}/\pi r_{\text{vasc}}^2$, where $K\phi_{\text{vasc}}$ and r_{vasc} denote the vessel volume fraction and the mean vessel radius (in mm), respectively. Values of MVD computed at the final time of our G-2022 model simulation were $\text{MVD} = 51.1\,\text{mm}^{-2}$ for the tumor and $97.2\,\text{mm}^{-2}$ for the normal tissue, actually falling within the experimentally measured range [7, 13]. For more simulations in critical cases, see [9].

Back to the time evolution of the model densities, the right panels of Figure 2, showing the spatial distribution of the growing neovasculature, emphasize that angiogenesis mostly develops in correspondence of the invading front. This is an important feature that the model helps to understand.

A striking model feature that emerges is that the solution behaves as a *TW* eventually replacing the no-tumor state with the state in which the tumor has invaded the whole

General parameters	
ϕ^*	0.85
p	1.1
V_c	$2.145 \cdot 10^{-9}$ cm^3
Λ	$8.0 \cdot 10^{-4}$ cm
r_0	$1.0 \cdot 10^{-3}$ cm
δ	$2 \cdot 10^{-4}$ cm
K	3.27
$K\phi_{v_a}$	$4.0 \cdot 10^{-3}$
λ_m	$2.08 \cdot 10^{-2}$ h^{-1}
Oxygen	
D_σ	$7.2 \cdot 10^{-2}$ cm$^2 \cdot$ h^{-1}
σ_h^*	$7.62 \cdot 10^{-5}$ M (= 60 mmHg)
σ_v^*	$4.45 \cdot 10^{-5}$ M (= 35 mmHg)
γ_h, γ_v	$1.86 \cdot 10^{-3}$ h^{-1} cm^3
A_{Hn}, A_{Hh}	$2.99 \cdot 10^{-13}$ mol $\cdot$ h^{-1}
K_{Hn}, K_{Hh}	$4.64 \cdot 10^{-6}$ M
Tumor and host tissue	
D_n, D_h, D_m	$3.6 \cdot 10^{-7}$ cm$^2 \cdot$ h^{-1}
A_χ	$2.88 \cdot 10^{-2}$ h^{-1}
K_χ	$5.08 \cdot 10^{-6}$ M (= 4 mmHg)
$\overline{\sigma}_n$	$2.54 \cdot 10^{-6}$ M (= 2 mmHg)
$\overline{\mu}_n$	$5\,(\ln 2/24) = 0.144$ h^{-1}
μ_0	$\ln 2/(10{\cdot}24) = 2.88 \cdot 10^{-3}$ h^{-1}
δ_h, δ_{v_h}	$4 \cdot 10^{-9}$ h$^{-1} \cdot$ cm^3
$\overline{\sigma}_h$	$3.81 \cdot 10^{-6}$ M (= 3 mmHg)
$\overline{\mu}_h$	$5\,(\ln 2/24) = 0.144$ h^{-1}
Angiogenesis and TAF	
ϕ_P^*	0.90
K_d	$5.75 \cdot 10^{-10}$ M
A_α	$2.88 \cdot 10^{-2}$ h^{-1}
A_β	$1.15 \cdot 10^{-1}$ h^{-1}
ν	1
D_P	$1.8 \cdot 10^{-3}$ cm$^2 \cdot$ h^{-1}
A_π	$5.96 \cdot 10^{-19}$ mol $\cdot$ h^{-1} (per cell)
K_π	$4.45 \cdot 10^{-5}$ M (= 35 mmHg)
A_C	$3.86 \cdot 10^{-19}$ mol $\cdot$ h^{-1} (per cell)
λ_P	0.65 h^{-1}
Vasculature	
γ	0.1 h^{-1}
K_q	$5 \cdot 10^4$ cm^{-1}
κ_{an}	$4 \cdot 10^{-9}$ cm$^3 \cdot$ cell$^{-1} \cdot$ h^{-1}
μ_v	$1.0 \cdot 10^{-3}$ h^{-1}
μ_w, μ_z	$5 \cdot 10^{-4}$ h^{-1}

TABLE 1. Parameter values used for the G-2022 model simulation (parameter sources specified in the reference paper [9]).

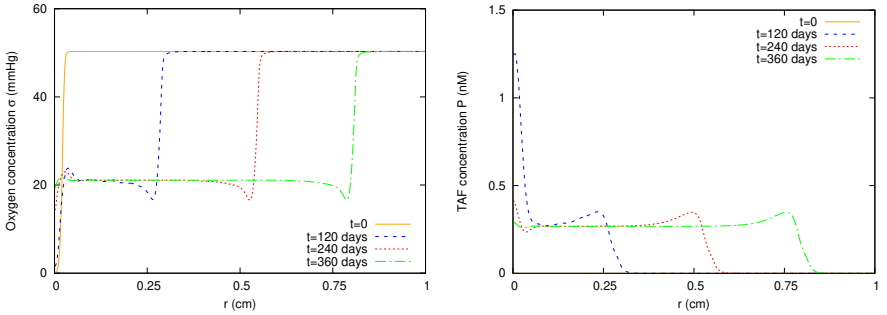

FIGURE 1. G-2022 model simulation of the chemical concentrations in a spherical domain with radius $R = 1$ cm after 4, 8, and 12 months. Left panel: oxygen (mmHg); right panel: TAF (nM). Parameters as in Table 1.

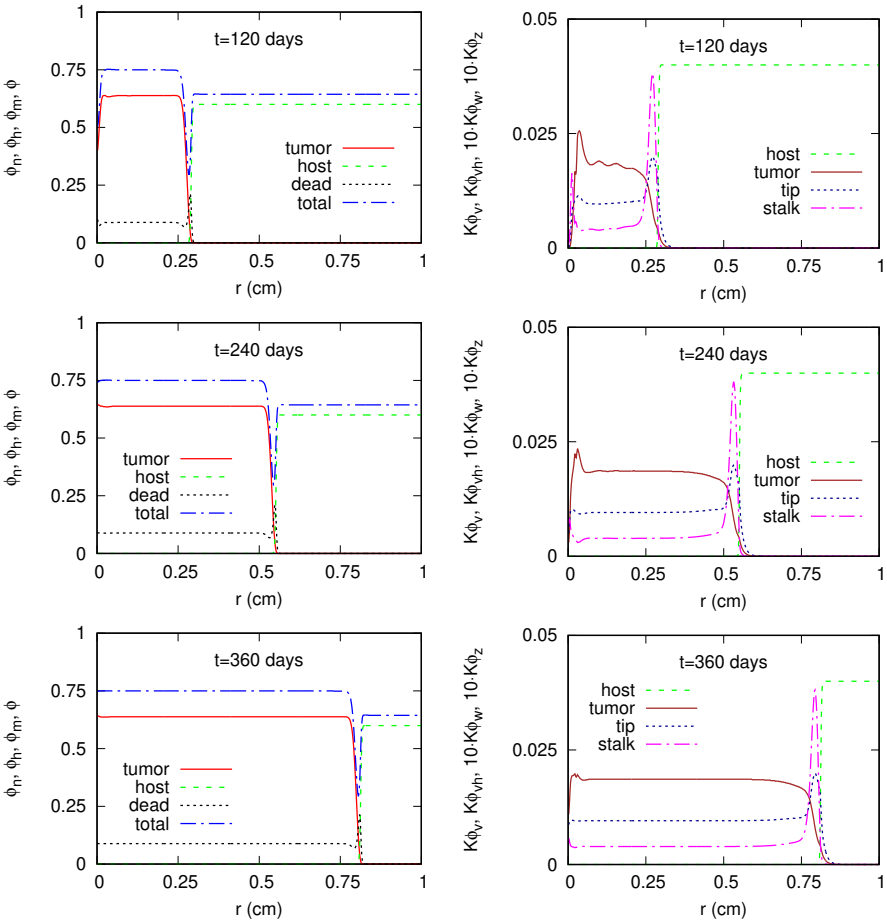

FIGURE 2. G-2022 model simulation of the local volume fractions of cells and vessels in a sphere of radius $R = 1$ cm after 4, 8, and 12 months. Left panels: host and tumor cells; right panels: host vessels, tumor vessels (mature, tip, and stalk). Parameters as in Table 1.

available space. So, as illustrated by Figures 1 and 2, the model provides information on the mean velocity of tumor invasion, which represents an important global parameter predictive of tumor aggressiveness. As pointed out in [9], the mean velocity of the advancing tumor is mainly related to the average cell diameter and proliferation rate. As a consequence of the increased diffusive mobility of cells, in the present simulation we get a velocity $\bar{c} = 21.8\,\mu$m/d, increased by about 10% with respect to the G-2021 model (19.8 μm/d). We also note that the maximal slope of ϕ_n, which occurs near the wave front, is $-29.9\,\text{cm}^{-1}$ ($-32.8\,\text{cm}^{-1}$ for model G-2021).

We believe that the TW behavior of the G-2022 model emerging from the previous analysis deserves a closer attention.

4. The TW structure

The first thing we have to notice is that, though the solution exhibits the structure of a TW, strictly speaking the model is not compatible with a TW solution. Let us try to replace the dependence on (r, t) by the dependence on the single variable $\eta = r - ct$. If we do that in equation (2.1) multiplied by the cell volume V_c and we use the simpler notations $y = \phi_n = nV_c$, $D = D_n$ dropping the arguments of the functions B, χ, μ, we obtain

$$-\Big(c + \frac{2}{r}DB\Big)y' = (DBy')' + B\chi y - \mu y, \tag{4.1}$$

where the prime denotes differentiation with respect to η. The term $2DB/r$ gives rise to an inconsistency which is obviously severe near the center. However, since the computed solution eventually develops almost rigorously into a TW moving with the speed $c = 21.8\,\mu\text{m/d} = 9.1 \cdot 10^{-5}\,\text{cm h}^{-1}$, the requirement $c \gg 2DB/r$ in (4.1) is fulfilled provided that $r \gg 2D/c = (7.2 \cdot 10^{-7})/(9.1 \cdot 10^{-5})$ cm, i.e., $r \gg 8.0 \cdot 10^{-3}$ cm. Hence this condition is satisfied already for $r > 0.1$ cm.

Of course such an argument could not work for the oxygen diffusion-consumption equation because of the large oxygen diffusivity, but we notice that, owing to its quasi-steady structure, the profile of σ is dragged along by v_h, v, n, h all possessing the TW structure dictated by y. A similar argument can be repeated for the other diffusing chemical quantity, namely P.

It is natural at this point to compare this result with the TWs obtained in the paper GG. The context of the latter paper was different for several important reasons: the geometry was 1-D; the tumor aggression to the host tissue was not direct but occurred through the rapidly diffusing H^+ ions entering the model with their own equation; death and proliferation rates were constant since the role of oxygen was disregarded; finally, angiogenesis was not considered. Thus we expect that some similarity may be present, but that of course there are also differences.

The first difference that one can notice is that the TW front in GG could or could not allow the simultaneous presence of tumor and healthy cells. Whether one or the other circumstance occurs depends on the relative size of various parameters, as pointed out in [6]. In the context of the present model instead, since the tumor aggression is expressed in (2.2) by the direct interaction term $-\delta_h n h$, the front can proceed only if both n and h are strictly positive, though it is not the aggression coefficient $-\delta_h$ which determines the TW propagation speed c.

Concerning the latter quantity, we may look instead for some similarity, since the underlying propagation mechanism both in our model and in the GG model is based on tumor cells diffusion and proliferation. A remarkable feature of the TWs in GG is that their propagation velocity has the following explicit expression:

$$c_{GG} = 2\,\mathrm{sqrt}(\chi_0 D_n),$$

where χ_0 is the tumor cell proliferation rate, which is constant in GG, and D_n is the tumor diffusion coefficient. We simulated the G-2022 model using different values of D_n, actually replicating very well the square root behavior. The value $\chi_0 = 4.8 \cdot 10^{-3}\,\mathrm{h}^{-1}$ [10] is to be compared with some value on the front of the proliferation rate in our solution, that is $B(\phi)\chi(\sigma)$. Looking at the values of ϕ and of σ on the TW front (Figures 1 and 2) we may say that $\chi(\sigma)$ is only slightly less than A_χ, thus, say, $2.5 \cdot 10^{-2}\,\mathrm{h}^{-1}$ while $B(\phi)$ takes values as low as 0.2 yielding that the product $B(\phi)\chi(\sigma)$ can actually approach a value similar to the one of χ_0. Discrepancies are attributable to the accumulation of dead cells on the front, which take a time of the order $1/\lambda_m$ to disappear. This is another reason for which our model and the GG model differ considerably ($B(\phi)$ varies a lot on the front while in the GG model the presence of dead cells was completely disregarded). Of course, increasing the parameter λ_m has the effect of making the TW solutions in the two models more similar. The result of repeated simulations as D_n or A_χ change is depicted in Figure 3 (left or right panel, respectively). Symbols with an overbar denote the baseline parameters of Table 1 and $\bar{c}$ the corresponding front velocity. Concerning the dependence of c on A_χ (see Figure 3, right panel), we note that the square root relationship is reproduced rather well by the model for lower proliferation rates, i.e., for $A_\chi/\bar{A}_\chi$ smaller than 1. On the contrary, when A_χ becomes greater than $\bar{A}_\chi$, an increased production of tumor cells occurs, thus depressing the parameters B and χ more consistently, with the consequence of slowing down the TW.

Going deeper into the TW structure of the solutions is exceedingly complicated because the model contains too many coupled equations. However, we can make some more considerations, starting from the front profile of the host tissue cells h. If in equation (2.2) we neglect the death by hypoxia, then in the TW framework the same

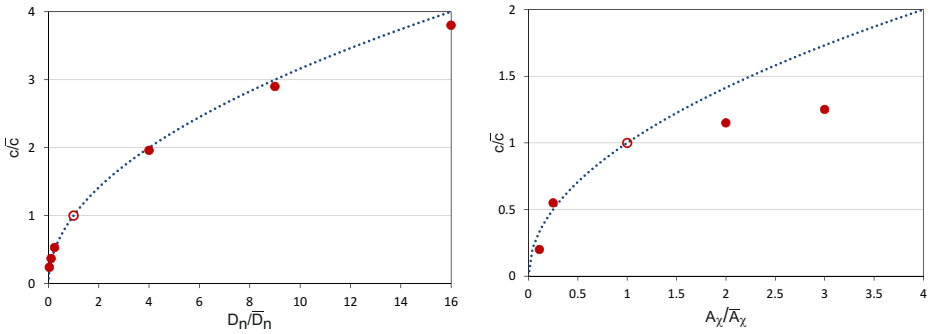

FIGURE 3. Dependence of the TW front speed c on D_n and on A_χ. Plot of the ratio between c and its baseline value $\bar{c}$ as a function of the normalized diffusion coefficient $D_n/\bar{D}_n$ (left panel) and of the normalized proliferation rate constant $A_\chi/\bar{A}_\chi$ (right panel). The baseline values used for normalization ($\bar{D}_n$, $\bar{A}_\chi$) are those of Table 1. Dots: computed values of $c/\bar{c}$, dotted line: square root of $D_n/\bar{D}_n$ (left) and $A_\chi/\bar{A}_\chi$ (right).

equation takes the form

$$-c\phi_h' = -\frac{\delta_h}{V_c}\phi_h y,$$

which leads to conclude that, for η within the front, it is

$$\phi_h(\eta) = \phi_{h\infty} \exp\left(-\frac{\delta_h}{cV_c} \int_\eta^\infty y(\xi)d\xi \right). \tag{4.2}$$

This equation shows that ϕ_h rapidly vanishes soon after the onset of $\phi_n = y$. Indeed, in the simulation we had $\delta_h/cV_c \simeq 2.5 \cdot 10^4\ \mathrm{cm}^{-1}$ and therefore a small average value of y (say 0.1) over a small portion of the wave front (say 10^{-3} cm) is enough to reduce the exponential in (4.2) below 0.1.

Based on this, we can say that ϕ_h can be neglected on the TW front. If in addition we also neglect all other cells volume fraction except ϕ_n, thus identifying ϕ with y in (23), where we drop the "foreign" term $2DB/r$, we find

$$-cy' = (DBy')' + B\chi y - \mu y, \tag{4.3}$$

where χ and μ are taken constant and $B = 1 - y/\phi^*$. Since the volume fractions ϕ_w, ϕ_z, ϕ_v are relatively small on the front, such a simplification makes sense if $\phi_m \ll 1$, i.e., if λ_m in equation (2.3) is large enough. This is actually the circumstance in which the profile of y on the TW front can be described by equation (4.3). For instance, we may look for the wave maximum slope $Y = \inf y'$, setting $y'' = 0$:

$$DY^2 - cY - \Phi = 0,$$

where $\Phi = B\chi y - \mu y$ is evaluated at the maximum slope point. Thus,

$$Y = c\phi^\star \frac{1 - \sqrt{1 + 4D\Phi/c^2}}{2D}. \tag{4.4}$$

As we said, the smaller the fraction ϕ_m the better the above approximation is, which can be obtained increasing λ_m to a few times its current baseline value ($2.08 \cdot 10^{-2}\,\mathrm{h}^{-1}$, [9]). Indeed, for λ_m four times as large as that value, the computed maximal slope of ϕ_n is $-29.8\,\mathrm{cm}^{-1}$, while $Y = -26.3\,\mathrm{cm}^{-1}$ with a -12% relative discrepancy.

It is easily seen that $dY/dc > 0$, i.e., the slower the wave, the steeper the front is. The same is true for the ϕ_h profile, which, according to (4.2), is regulated by the ratio $\delta_h/(cV_c)$.

5. An FB scheme replacing the TW model

We consider now the limit case in which the healthy cells die instantly when reached by the tumor cells. In that situation, the tumor invasion front $r = \rho(t)$ separates the tumor region $0 < r < \rho(t)$, in which $n > 0$ and $h \equiv 0$, from the healthy tissue ($n \equiv 0$, $h \equiv h_0$, and $m \equiv 0$, since σ is above the death threshold).

Thus, we no longer have to deal with the equation for h. All the equations governing the other quantities remain the same including the one for v_h (we cannot put $v_h = 0$ in the tumor region because part of the original vasculature has to survive for some time in order to boost angiogenesis).

Consistently with the assumption made on the death of healthy cells, we assume that

$$m\big(\rho(t), t\big) = h_0. \tag{5.1}$$

Concerning the population n, we say that on the front the corresponding incoming cell flux equals the cell density current created by the front displacement

$$-D_n B(\phi)\frac{\partial n}{\partial r} = n\dot{\rho}, \quad r = \rho(t), \tag{5.2}$$

and that the front speed is proportional to the tumor volume fraction ϕ_n

$$\dot{\rho} = \Theta\phi_n, \quad r = \rho(t), \tag{5.3}$$

for some positive constant Θ.

The target is to choose Θ so that $\dot{\rho}$ turns out to be comparable with the known TW front speed.

To sum up, in the FB model the equations for n and m keep the same form of equations (2.1) and (2.3), which now hold for $0 < r < \rho(t)$. Concerning the related boundary conditions, in addition to the usual zero flux condition at $r = 0$, we prescribe at $r = \rho(t)$ the conditions (5.2) and (5.1) for n and m, respectively. The healthy tissue dynamic is described by the pair of conditions (i) $h \equiv 0$, for $0 < r < \rho(t)$ and (ii) $h \equiv h_0$, for $\rho(t) \leq r < R$. The evolution of the vasculature (either normal and tumoral) is still described by (2.4) and (2.7)–(2.9) to be complemented with the same boundary conditions of the G-2022 model for $r \in (0, R)$ and $t \in (0, T)$. The initial distributions are assigned similarly to the paper [9].

REMARK. As before, the chemical species σ and P, along with the cellular species triggering chemotaxis and angiogenesis, are allowed to diffuse in the whole domain.

The FB model equations were solved numerically in a spherical domain with assigned radius R and over a time interval of length T, by means of a routine implementing a finite difference scheme similar to that developed for the TW model. Concerning the parabolic PDEs of the model, the routine exploited an explicit, forward in time, centered in space method that proved to be numerically stable and capable of reproducing the G-2022 model behavior for reasonably wide ranges of the parameter values. Figure 4 reports the numerical solutions of the FB model computed assuming for the common parameters the values previously used for the TW model (see Table 1) with the exception of λ_m, which was increased by four times with respect to the baseline value to favor the removal of dead cells. As for the new parameter Θ, which has the dimension of a velocity, we set $\Theta = 2.0 \cdot 10^{-4}$ cm/h. With this choice, and supposing an initial tumor volume fraction $\bar{\phi}_n$ equal to 0.6, in view of (5.3), we expect to get a front velocity actually about 25% greater than the reference one obtained by the G-2022 model ($\bar{c} = 9.1 \cdot 10^{-5}$ cm/h). Setting the mentioned value of Θ is motivated by a following quantitative comparison between the FB model and the G-2022 (see the end of the present section). In fact, the FB model can be considered as a limit case of a G-2022 model characterized by higher δ_h and λ_m, i.e., increased tumor aggression rate and decay of dead cells, with respect to the baseline parameter setting. So, the velocity increment consequent to the choice of Θ is consistent with the FB scheme assumptions and, in particular, it should reflect a parallel acceleration of the tumor invasion in the TW model.

The FB model local volume fractions of cells and vessels are shown in Figure 4. From a computational point of view, we observe that the FB model offers some advantage with respect to the TW model, in terms of computation time. This is actually due to the fact that we need not solve the diffusion equation for h, while the equations for n and m can be solved over a portion of the whole domain, i.e., for $r \in (0, \rho)$. Another favorable

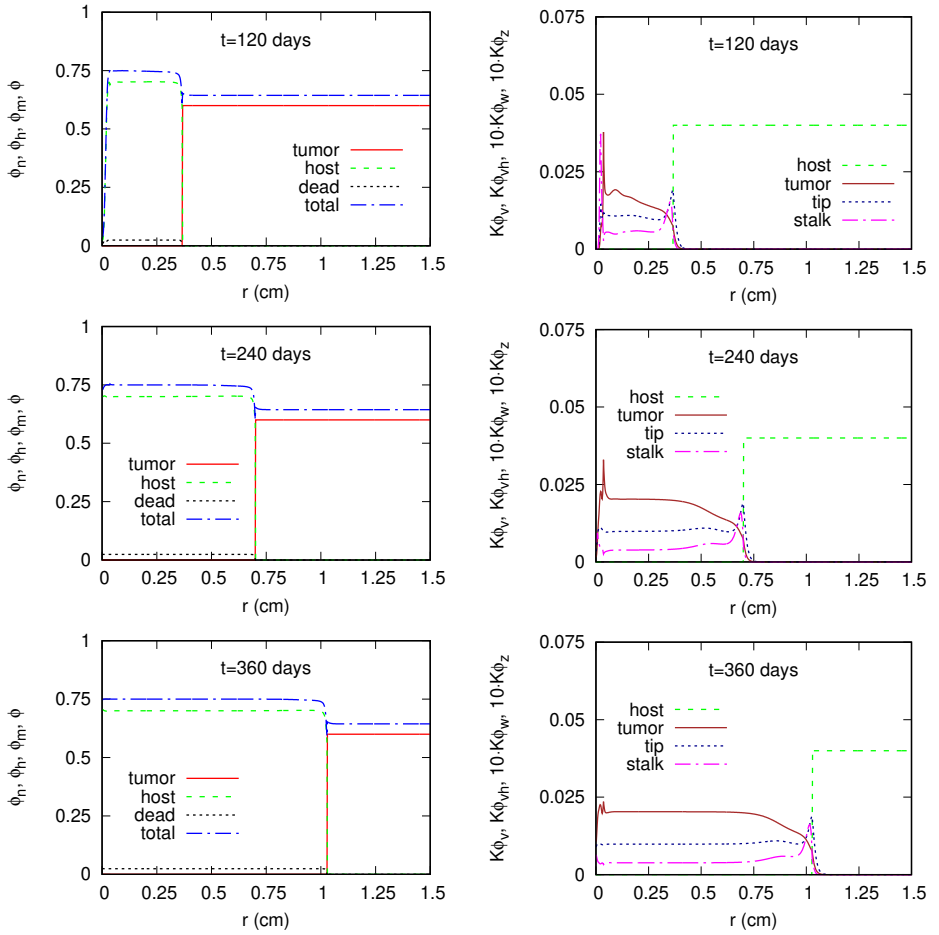

FIGURE 4. FB model simulation. Evolution of the local volume fractions of cells and of vessels in a sphere of radius $R = 1.5\,\text{cm}$ after 4, 8, and 12 months, with $\Theta = 2.0 \cdot 10^{-4}$ cm/h. Left panels: host and tumor cells; right panels: host vessels, tumor vessels (mature, tip, and stalk).

aspect of the FB model is that using equation (5.3) allows to estimate $\dot{\rho}(t)$ and then to predict the evolution of the outer growing tumor radius $\rho(t)$ (or tumor volume).

For a punctual comparison of the two models, we performed one more simulation of the TW model, in which a higher tumor aggression rate δ_h and a higher dead cell degradation rate λ_m were assumed to match the profiles obtained by the FB model and, at the same time, to verify the effectiveness of the FB approximation. So, the next figure (Figure 5), to be compared with Figure 4, gives an example with $\delta_h = 1.0 \cdot 10^{-8}\,\text{h}^{-1}\,\text{cm}^3$ and $\lambda_m = 8.32 \cdot 10^{-2}\,\text{h}^{-1}$ (fourfold the baseline value). Concerning the TW model, we incidentally observe that, as expected, the velocity of the TW propagating front increases up to 28.7 μm/d, whereas the front slope decreases becoming $-27.5\,\text{cm}^{-1}$,

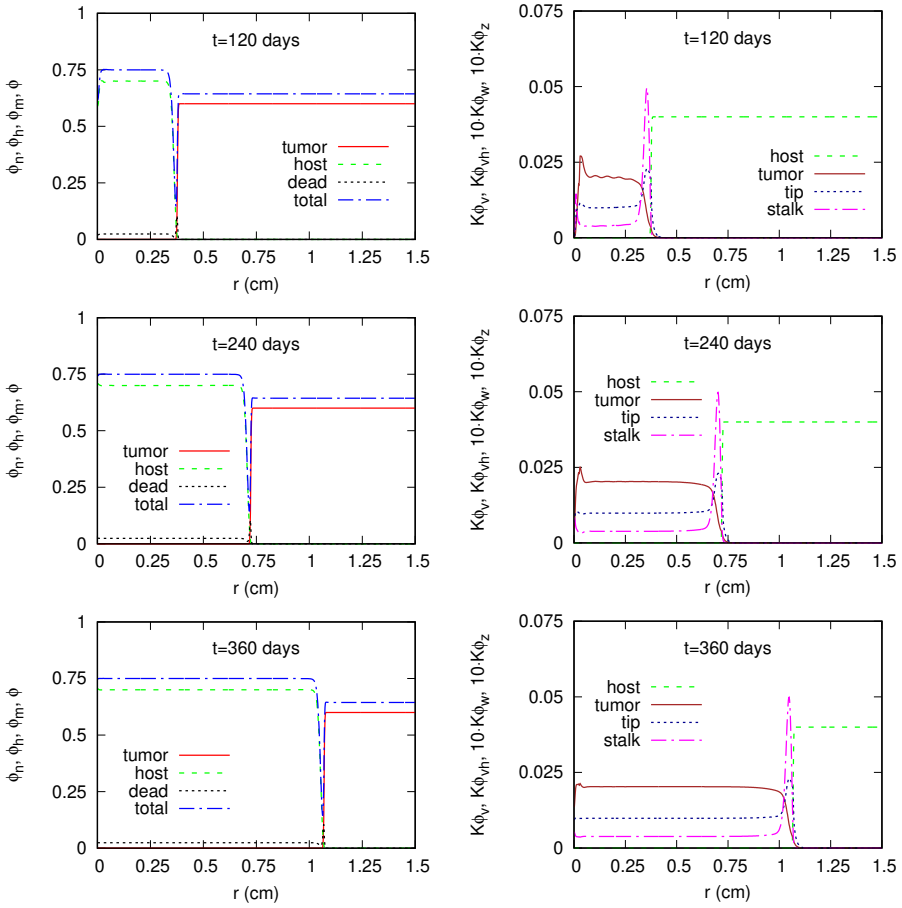

FIGURE 5. TW model simulation. Evolution of the local volume fractions of cells and of vessels in a sphere of radius $R = 1.5$ cm after 4, 8, and 12 months. Parameter values as in Table 1, except $\delta_h = 1.0 \cdot 10^{-8}\,\mathrm{h}^{-1} \cdot \mathrm{cm}^3$ and $\lambda_m = 8.32 \cdot 10^{-2}\,\mathrm{h}^{-1}$. Left panels: host and tumor cells; right panels: host vessels, tumor vessels (mature, tip, and stalk).

mainly because of the increase of δ_h. It can be also noted that, owing to the increase of λ_m, the fraction of dead cell is about halved with respect to the reference simulation of Figure 2.

It can be observed that although the volume fraction profiles generated by the FB model are not identical to the TW ones, the main features of all quantities appear to be conserved. In particular, for both models the formation of tumor vessels occurs mainly right behind the invasion front, even though in the FB model the angiogenic activity appears to be concentrated near the front and followed by a stabilizing "tail" that tends to the asymptotic value.

Quantity	FB (Figure 4)	TW (Figure 5)
ρ (cm)	1.03	1.05
$\bar{c}$ (μm/d)	28.6	28.7
ϕ_n	0.70	0.70
ϕ	0.75	0.75
ϕ_m	$2.43 \cdot 10^{-2}$	$2.42 \cdot 10^{-2}$
$K\phi_v$	$2.03 \cdot 10^{-2}$	$2.03 \cdot 10^{-2}$
$K\phi_w$	$9.86 \cdot 10^{-4}$	$9.85 \cdot 10^{-4}$
$K\phi_z$	$3.83 \cdot 10^{-4}$	$3.82 \cdot 10^{-4}$

TABLE 2. Quantitative comparison of the FB vs. TW model by means of the comparison of relevant quantities computed at $t = 360$ days.

Moreover, completing the quantitative comparison between the FB and the TW model, Table 2 reports the values of corresponding quantities computed by the two models for $t = 360$ days, indicating an excellent agreement of the numerical values of the respective asymptotic states.

Let us conclude this section by envisaging a slight extension of the FB model that would make it possible to account for incorporating the variability of the cell diffusion coefficient. Indeed, as noted in Section 4 with regard to the TW model, an interesting property of the TW front speed c is its dependence on the square root of the parameter D_n. This suggests to modify the expression (5.3) of $\dot{\rho}(t)$ as follows. We start from the observation that the product cn must coincide with the flux of n at the front and that the flux can be approximated by $DB(\phi)Y$, taking for Y the expression (4.4), which has been seen to provide a sufficiently accurate approximation of $\partial\phi_n/\partial r$ for suitable parameter ranges. Now, c has been shown to be proportional to $D_n^{1/2}$ and we have n proportional to YD_n/c. Then, recalling that Y is proportional to c/D_n, the behavior of $d\rho/dt$, with respect to the diffusion coefficient, is the same of Θ. Hence, the suggested extension consists in taking $\Theta = \overline{\Theta}\,\mathrm{sqrt}(D_n/\overline{D}_n)$, so as to obtain automatically for $\dot{\rho}$ the same dependence of c on D_n itself.

6. CONCLUDING REMARKS

- Some model refinement was incorporated in the original G-2021 model, still conserving the essential structure and properties. Precisely, all cell types (healthy, tumor, and dead) of the present model are endowed with diffusive mobility.
- A further analysis of the solution behavior as a TW, and of its dependence on some critical biological parameters was performed.
- An alternative model was formulated to represent the tumor invasion by means of an FB representing the outer boundary of a growing tumor mass. The new formulation

matches the results of the previous model in a biologically significant range of the parameters.

- The proposed FB model provides an expression representing the evolution of the tumor radius, or equivalently tumor volume, at least in a first, initial phase of tumor vasculature development. Therefore, in the same initial phase, the FB model could be used to include the effect of antiangiogenic therapies, following the framework of the seminal model in [11] and studies like e.g. [4, 5].

References

[1] T. Adair – J. Montani, *Angiogenesis*. Morgan & Claypool Life Sciences, 2010.

[2] A. Anderson – M. Chaplain, Continuous and discrete mathematical models of tumor-induced angiogenesis. *Bull. Math. Biol.* **60** (1998), no. 5, 857–899. Zbl 0923.92011

[3] D. Balding – D. McElwain, A mathematical model of tumour-induced capillary growth. *J. Theoret. Biol.* **114** (1985), 53–73.

[4] A. d'Onofrio – A. Gandolfi, Tumour eradication by antiangiogenic therapy: analysis and extensions of the model by Hahnfeldt et al. (1999). *Math. Biosci.* **191** (2004), no. 2, 159–184. Zbl 1050.92039 MR 2090896

[5] A. d'Onofrio – A. Gandolfi, A family of models of angiogenesis and anti-angiogenesis anti-cancer therapy. *Math. Med. Biol.* **26** (2008), 63–95.

[6] A. Fasano – M. A. Herrero – M. R. Rodrigo, Slow and fast invasion waves in a model of acid-mediated tumour growth. *Math. Biosci.* **220** (2009), no. 1, 45–56. Zbl 1178.35120 MR 2542100

[7] J. Forster – W. Harriss-Phillips – M. Douglass – E. Bezak, A review of the development of tumor vasculature and its effects on the tumor microenvironment. *Hypoxia* **5** (2017), 21–32.

[8] T. Gallay – C. Mascia, Propagation fronts in a simplified model of tumor growth with degenerate cross-dependent self-diffusivity. *Nonlinear Anal. Real World Appl.* **63** (2022), article no. 103387. Zbl 1483.35066 MR 4296247

[9] A. Gandolfi – S. De Franciscis – A. d'Onofrio – A. Fasano – C. Sinisgalli, Angiogenesis and vessel co-option in a mathematical model of diffusive tumor growth: the role of chemotaxis. *J. Theoret. Biol.* **512** (2021), article no. 110526. MR 4202591

[10] R. Gatenby – E. Gawlinski, A reaction-diffusion model of cancer invasion. *Cancer Res.* **56** (1996), 5745–5753.

[11] P. Hahnfeldt – D. Panigrahy – J. Folkman – L. Hlatky, Tumor development under angiogenic signaling: a dynamical theory of tumor growth, treatment response, and post-vascular dormancy. *Cancer Res.* **59** (1999), 4770–4775.

[12] T. Hillen – K. J. Painter, A user's guide to PDE models for chemotaxis. *J. Math. Biol.* **58** (2009), no. 1-2, 183–217. Zbl 1161.92003 MR 2448428

[13] J. Kather – A. Marx – C. Reyes-Aldasoro – L. Schad – F. Zöllner – C. Weis, Continuous representation of tumor microvessel density and detection of angiogenic hotspots in histological whole-slide images. *Oncotarget* **6** (2015), 19163–19176.

[14] E. Keller – L. Segel, Model for chemotaxis. *J. Theoret. Biol.* **30** (1971), no. 2, 225–234. Zbl 1170.92307

[15] N. Lai – H. Zhou – G. Saidel – M. Wolf – K. McCully – L. Gladden – M. Cabrera, Modeling oxygenation in venous blood and skeletal muscle in response to exercise using near-infrared spectroscopy. *J. Appl. Physiol.* **106** (2009), 1858–1874.

[16] H. G. Othmer – S. R. Dunbar – W. Alt, Models of dispersal in biological systems. *J. Math. Biol.* **26** (1988), no. 3, 263–298. Zbl 0713.92018 MR 949094

[17] C. S. Patlak, Random walk with persistence and external bias. *Bull. Math. Biophys.* **15** (1953), 311–338. Zbl 1296.82044 MR 81586

[18] M. Rivero – R. Tranquillo – H. Buettner – D. Lauffenburger, Transport models for chemotactic cell populations based on individual cell behavior. *Chem. Eng. Sci.* **44** (1989), 2881–2897.

[19] M. Scianna – L. Munaron – L. Preziosi, A multiscale hybrid approach for vasculogenesis and related potential blocking therapies. *Prog. Biophys. Mol. Biol.* **106** (2011), 450–462.

[20] A. Tosin – D. Ambrosi – L. Preziosi, Mechanics and chemotaxis in the morphogenesis of vascular networks. *Bull. Math. Biol.* **68** (2006), no. 7, 1819–1836. Zbl 1334.92066 MR 2257726

[21] R. Tranquillo – D. Lauffenburger – S. Zigmond, A stochastic model for leukocyte random motility and chemotaxis based on receptor binding fluctuations. *J. Cell Biol.* **106** (1988), no. 2, 303–309.

Received 1 July 2022,
and in revised form 5 September 2022

Antonio Fasano
Dipartimento di Matematica “Ulisse Dini”, Università degli Studi di Firenze,
Viale Morgagni 67/a, 50134 Firenze;
FIAB SpA,
Via Bruno Passerini 2, 50039 Vicchio; and
Istituto di Analisi dei Sistemi ed Informatica “A. Ruberti” - CNR,
Via dei Taurini 19, 00185 Roma, Italy
a.fasano@fiab.it

Carmela Sinisgalli
Istituto di Analisi dei Sistemi ed Informatica “A. Ruberti” - CNR,
Via dei Taurini 19, 00185 Roma, Italy
carmela.sinisgalli@iasi.cnr.it